Research Square

Preprints are preliminary reports that have not undergone peer review. They should not be considered conclusive, used to inform clinical practice, or referenced by the media as validated information.

Improving Quantum-to-Classical Data Decoding using Optimized Quantum Wavelet Transform

Mingyoung Jeng (mingyoungjeng@ku.edu)
University of Kansas

SM Ishraq Ul Islam
University of Kansas

David Levy
University of Kansas

Andrew Riachi
University of Kansas

Manu Chaudhary
University of Kansas

Md. Alvir Islam Nobel
University of Kansas

Dylan Kneidel
University of Kansas

Vinayak Jha
University of Kansas

Jack Bauer
University of Kansas

Anshul Maurya
Florida Institute of Technology

Naveed Mahmud
Florida Institute of Technology

Esam El-Araby
University of Kansas

Research Article

Keywords: Quantum Computing, Quantum Algorithms, Quantum State Preparation and Measurement

Posted Date: April 5th, 2023

DOI: https://doi.org/10.21203/rs.3.rs-2763569/v1

License: This work is licensed under a Creative Commons Attribution 4.0 International License.
Read Full License

Additional Declarations: No competing interests reported.

Improving Quantum-to-Classical Data Decoding using Optimized Quantum Wavelet Transform

Mingyoung Jeng[1*], SM Ishraq Ul Islam[1], David Levy[1], Andrew Riachi[1], Manu Chaudhary[1], Md. Alvir Islam Nobel[1], Dylan Kneidel[1], Vinayak Jha[1], Jack Bauer[1], Anshul Maurya[2], Naveed Mahmud[2], Esam El-Araby[1]

[1*]Department of Electrical Engineering and Computer Science, University of Kansas, Lawrence, KS, 66045, USA.
[1]Department of Electrical Engineering and Computer Science, University of Kansas, Lawrence, KS, 66045, USA.
[2]Department of Computer Engineering and Sciences, Florida Institute of Technology, Melbourne, FL, 32901, USA.

*Corresponding author(s). E-mail(s): mingyoungjeng@ku.edu; Contributing authors: ishraq@ku.edu; david.levy@ku.edu; ariachi@ku.edu; manu.chaudhary@ku.edu; islam.alvir@ku.edu; dckneidel@ku.edu; vinayakjha@ku.edu; jack.bauer@ku.edu; amaurya2022@my.fit.edu; nmahmud@fit.edu; esam@ku.edu;

Abstract

One of the challenges facing current Noisy-Intermediate-Scale-Quantum devices (NISQ) is achieving efficient quantum circuit measurement or readout. The process of extracting classical data from the quantum domain, termed in this work as quantum-to-classical (Q2C) data decoding, generally incurs significant overhead, since the quantum circuit needs to be sampled repeatedly to obtain useful data readout. In this paper, we propose and evaluate time-efficient and depth-optimized Q2C methods based on the multidimensional, multilevel-decomposable, quantum wavelet transform (QWT) whose packet and pyramidal forms are leveraged and optimized. We also propose a zero-depth technique that uses selective placement of measurement gates to perform the QWT operation. To demonstrate their efficiency, the proposed techniques are quantitatively evaluated in terms of execution time, circuit depth, and accuracy in comparison to

existing Q2C techniques. Experimental evaluations of the proposed Q2C methods are performed using real high-resolution multispectral images on a 27-qubit state-of-the-art quantum computing device from IBM Quantum.

Keywords: Quantum Computing, Quantum Algorithms, Quantum State Preparation and Measurement

1 Introduction

Quantum computers can take advantage of unique quantum mechanical properties, i.e., superposition and entanglement, to achieve speedup in computation [1] over classical computers for specific problems such as large integer factorization and unstructured database search [2, 3]. Nevertheless, existing noisy intermediate-scale quantum (NISQ) devices have limited practical applications [4] due to critical challenges [5], such as decoding meaningful classical data from the quantum domain. For example, in applications like quantum image processing, where information is usually encoded as quantum state amplitudes [6], repeated sampling of the quantum circuit is required to generate a probability distribution from which the processed image data can be recovered [7]. The process of obtaining data from the quantum domain, henceforth called quantum-to-classical (Q2C) data decoding, introduces significant overhead in the circuit execution time, necessitating further investigation of time-efficient data decoding methods.

In this paper, we propose and evaluate techniques for efficient Q2C data decoding based on the multidimensional, multilevel-decomposable quantum wavelet transform (QWT) [8, 9, 10, 11]. In our work, we investigate and optimize the quantum Haar transform (QHT) for performing multidimensional and multilevel decomposition in either packet or pyramidal form. When applying QHT to the output of a quantum circuit, we show that the resulting quantum state can be represented with fewer qubits by reducing its dimensionality from a higher-dimensional space to a lower-dimensional space. Multilevel-decomposable QHT has been proven to be effective for reducing the dimensionality of high-resolution spatio-spectral data while maintaining spatial and temporal locality [12]. It is also reported that sampling a lower-dimensional space reduces execution time, thus improving the Q2C decoding process [8]. We also present the quantum circuits and accompanying circuit depth analysis corresponding to the proposed QHT-based approach, demonstrating its space and time efficiency. From these circuits, we derived a highly depth-optimized technique that is capable of performing the QHT operation without a supplementary quantum circuit, which we call 'measurement-based' QHT decomposition. In this approach, the measurement of select qubits allows us to sample the representative output data in a lower-dimensional space.

The proposed quantum methods and circuits for Q2C are evaluated on the `Qiskit` SDK from IBM Quantum [13] using their general-purpose Aer simulator and *ibmq_toronto* quantum device. By experimentally determining circuit depth, calculating data correlation, and measuring execution time, a quantitative comparison of the proposed Q2C methods with state-of-the-art techniques is presented. Additionally, the proposed Q2C methods are compared with a reported Q2C readout technique based

on the quantum Fourier transform (QFT) [14]. The experimental results show that our proposed methods are more time and space efficient compared to existing methods.

The rest of the paper is organized as follows. Section 2 discusses background concepts and related work. Section 3 presents the proposed method and quantum circuits. Section 4 shows the experimental work and results with accompanying analysis. Finally, Section 5 concludes our work and discusses potential future work.

2 Background and Related Work

In this section, we discuss basic quantum concepts in addition to the fundamental quantum gates used for Q2C data decoding. Related work will also be discussed.

In this paper, we will utilize the following mathematical notation to describe leveraged quantum concepts. An n-qubit quantum state $|\psi_n\rangle$ can be represented by a normalized statevector of $N = 2^n$ complex state amplitudes/coefficients $c_i \in \mathbb{C}$ where $0 \leq i < N$, as shown in (1).

$$|\psi_n\rangle = \sum_{i=0}^{N-1} c_i \, |i\rangle = \begin{bmatrix} c_0 \\ c_1 \\ \vdots \\ c_i \\ \vdots \\ c_{N-2} \\ c_{N-1} \end{bmatrix}, \text{ where } \langle\psi_n|\psi_n\rangle = \sum_{i=0}^{N-1} |c_i|^2 = 1, \text{ and } 0 \leq i < N \tag{1}$$

2.1 Quantum Gates

This subsection details the function, matrix representation, and gate representation for the various quantum gates that are used in our proposed circuits.

Hadamard Gate

The Hadamard gate [14] is a single-qubit gate, as described by (2), that can be used to create a superposition of the $|0\rangle$ and $|1\rangle$ basis states.

$$H \equiv \frac{1}{\sqrt{2}} \begin{bmatrix} 1 & 1 \\ 1 & -1 \end{bmatrix} = \text{—}\boxed{\mathbf{H}}\text{—} \tag{2}$$

SWAP Gate

The SWAP gate is a two-qubit quantum gate, as described by (3), that exchanges the states of the two input qubits, e.g., applying the SWAP operation on the $|q_1 q_0\rangle$ state would result in the state $|q_0 q_1\rangle$.

$$\text{SWAP} \equiv \begin{bmatrix} 1 & 0 & 0 & 0 \\ 0 & 0 & 1 & 0 \\ 0 & 1 & 0 & 0 \\ 0 & 0 & 0 & 1 \end{bmatrix} = \tag{3}$$

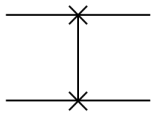

Quantum Rotate-Left (RoL) and Rotate-Right (RoR) Operations

We define the Rotate-Left (RoL) and Rotate-Right (RoR) gates as specialized permutation operations that perform a cyclic rotation, i.e., perfect-shuffle, of the input qubits, as shown in Fig. 1. Each gate can be constructed of SWAP gates, where a perfect-shuffle operation over n qubits necessitates $n-1$ SWAP gates in series, see Fig. 1.

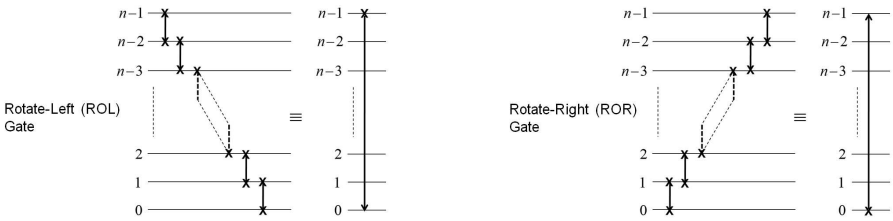

$\text{RoL}(|q_{n-1}q_{n-2}\ldots q_0\rangle) = |q_{n-2}\ldots q_0 q_{n-1}\rangle$ $\quad$ $\text{RoR}(|q_{n-1}\ldots q_1 q_0\rangle) = |q_0 q_{n-1}\ldots q_1\rangle$

Fig. 1: Rotate-Left (RoL) and Rotate-Right (RoR) gates

Measurement Gate

Measuring (observing) qubits is a non-unitary (irreversible) operation. A measurement (readout) gate is a single qubit operation that assigns the observed quantum state $|\psi_1\rangle$ to a single value. In other words, a measurement gate projects the quantum state to one of its basis states, i.e., $|0\rangle$ or $|1\rangle$ for a single-qubit state, with a probability equal to the square of the magnitude of the basis state coefficient, i.e., $p_0 = |c_0|^2$, and $p_1 = |c_1|^2$, see (4).

$$P(\psi_1) = \begin{bmatrix} p_0 \\ p_1 \end{bmatrix} = \begin{bmatrix} |c_0|^2 \\ |c_1|^2 \end{bmatrix} = \tag{4}$$

In general, when all qubits of a quantum state $|\psi_n\rangle$ in an n-qubit quantum circuit are fully measured, the probability of finding the qubits in a given state $|i\rangle$ is given by $|c_i|^2$, and the full-measurement probability distribution of finding the qubits in all possible states can be expressed as $P(\psi_n)$, see (5a) and Fig. 2a. When excluding a partial subset m qubits of the n qubits from measurements, the partial-measurement probability distribution can be expressed as a conditional probability $P(\psi_n \mid q_m ... q_1 = \times ... \times)$, where each unmeasured qubit q_m could arbitrarily be in a 'don't care' state, i.e., $\times \equiv 0$ or 1. Equation (5b) and Fig. 2b show an example of one qubit, i.e., the least-significant qubit q_0, being excluded from the partial-measurement of the remaining

$n-1$ qubits. It is worth mentioning that for every m qubits that are excluded from the partial-measurements, the number of measured basis states and consequently the size of the partial-measurement probability distribution is reduced by a factor of 2^m, i.e., being equal to $N/2^m = 2^{(n-m)} = 2^k$ where $k = n - m$ is the number of measured qubits, see (5b) and Fig. 2b.

$$P(\psi_n) = \begin{bmatrix} p_0 \\ p_1 \\ \vdots \\ p_i \\ \vdots \\ p_{N-2} \\ p_{N-1} \end{bmatrix} = \begin{bmatrix} |c_0|^2 \\ |c_1|^2 \\ \vdots \\ |c_i|^2 \\ \vdots \\ |c_{N-2}|^2 \\ |c_{N-1}|^2 \end{bmatrix}, \text{ where } P(\psi_n = i) = p_i = |c_i|^2, \text{ and } 0 \leq i < N \tag{5a}$$

$$P(\psi_n \mid q_0 = \times) = \begin{bmatrix} p_{0|q_0} \\ \vdots \\ p_{i|q_0} \\ \vdots \\ p_{\frac{N}{2}-1|q_0} \end{bmatrix} = \begin{bmatrix} |c_0|^2 + |c_1|^2 \\ \vdots \\ |c_{2i}|^2 + |c_{2i+1}|^2 \\ \vdots \\ |c_{N-2}|^2 + |c_{N-1}|^2 \end{bmatrix}, \text{ where} \tag{5b}$$

$$P(\psi_n = i \mid q_0 = \times) = p_{i|q_0} = |c_{2i}|^2 + |c_{2i+1}|^2, \text{ and } 0 \leq i < \frac{N}{2}$$

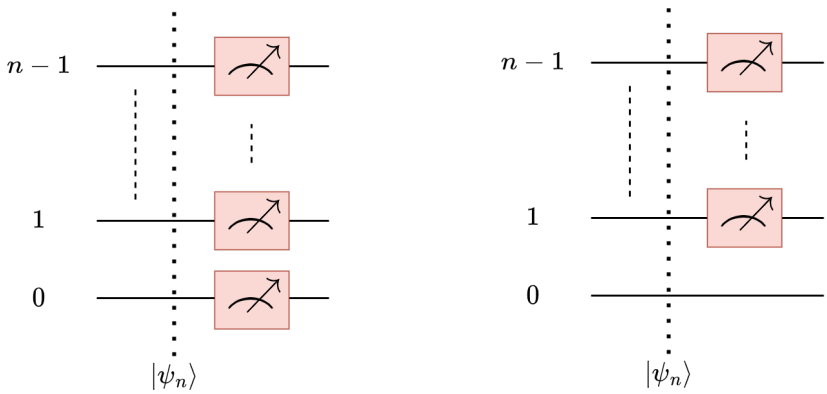

(a) Full-measurement of n qubits (b) Partial-measurement of $n-1$ qubits

Fig. 2: Measurements of an n-qubit quantum state $|\psi_n\rangle$

2.2 Circuit Depth

The depth of a quantum circuit is calculated from the critical path that has the largest propagation delay accumulated from cascaded gates through the circuit. Quantum circuits also accumulate gate errors throughout their runtime [15] which compound with deeper circuits. Therefore, circuit depth determines the total execution time of the quantum circuit on a physical device and is often used as a metric for quantitatively evaluating the speed and performance of quantum circuits. In addition, it could be utilized as a useful indication for the quality of results (fidelity) of quantum circuits. Therefore, minimizing/optimizing circuit depth would result in performance and fidelity improvements [15]. However, the magnitude of gate delay and error vary depending on the type of gate operation, e.g., H, SWAP, etc. Thus, without considering those differences, depth alone can only provide a speculative analysis of a circuit's execution time and result fidelity.

In a previous work [11], we described how to use circuit depth analysis to calculate the expected execution time on a physical quantum device. In this work, we extend our analysis to further optimize the depth of the proposed circuits where different operations are executed in parallel on the same circuit layer.

2.3 Quantum Haar Transform

In the classical domain, a discrete wavelet transform (DWT) decomposes signals/data into its spatio-temporal spectral components using non-sinusoidal functions called mother wavelets [16]. DWT can be applied to perform dimension reduction, as shown in Fig. 3, by separating multidimensional data into its low-frequency and high-frequency components [16, 17]. The isolated low-frequency terms are usually used to represent a compressed/decomposed output where the size of each dimension of the output data is reduced by a factor of 2^ℓ, where ℓ is the number of decomposition levels [17]. If the high-frequency terms are preserved, a complete reconstruction of the original input can be accomplished via the inverse operation, see Fig. 3. The Haar wavelet transform is one of the fundamental wavelet transforms, utilizing a mother wavelet that can be constructed using a basic unit step function $u(t)$ [11]. The Haar transform can be performed in either packet decomposition or pyramidal decomposition form, differentiated by how multiple levels of decomposition are performed. After the initial level of decomposition, packet decomposition performs subsequent levels of decomposition on both the low-frequency and high-frequency components, while pyramidal decomposition restricts further decomposition to only the low-frequency components [16, 18].

$$|\psi\rangle_{\text{QHT}} = \frac{1}{\sqrt{N}} \sum_{i=0}^{N-1} \sum_{q=0}^{N-1} f(q \cdot \Delta t) \Psi_D \left(\frac{q-j}{K} \right) |i\rangle \tag{6}$$

Similar to the classical DWT, quantum circuits can be developed to perform the so-called quantum Haar transform (QHT) [9, 10, 11]. For QHT circuits, the input data samples are generally encoded as the amplitudes of a superimposed input quantum state $|\psi\rangle$. The Haar function is then applied on the state amplitudes, resulting in the state represented by (6), where Ψ_D is the discrete Haar mother wavelet [11], Δt is the

(a) 1-level decomposition (scaled-up) (b) 3-level decomposition (scaled-up) (c) 5-level decomposition (scaled-up) (d) 7-level decomposition (scaled-up)

(e) 1-level reconstruction (f) 3-level reconstruction (g) 5-level reconstruction (h) 7-level reconstruction

Fig. 3: Decomposition and reconstruction of a $(4096 \times 4096 \times 3)$ image using the 2D Haar wavelet transform

sampling period, K is the Haar window size in samples, and N is the number of data samples. The specific quantum circuits are discussed in further detail in Section 3.2.

2.4 Related Work

Conventional quantum-to-classical (Q2C) data decoding for a given quantum circuit, as shown in Fig. 4, obtains the complete quantum state of a circuit by performing repeated circuit sampling, also known as 'shots'. The measurements are used to construct a probability distribution of the possible discrete basis states, where the normalized frequency of measurements represent the square of the magnitudes of the output quantum state coefficients. The number of repeated measurements correlates with the accuracy of the data relative to the expected output quantum state. Generally, a large number of repeated circuit sampling is required to improve the accuracy of measurements and minimize the effects of statistical noise, which adds a significant overhead to the total circuit execution time.

To minimize the overhead of repeated circuit sampling, algorithms can be appended to a circuit immediately prior to measurement, which typically will attempt to decrease either the number of measured qubits or the number of required shots to sample the quantum state. In [14], the authors proposed a Q2C data decoding technique leveraging the quantum Fourier transform (QFT) algorithm to sample the quantum circuit output in the Fourier basis and extract a collective property of the amplitude data, see Fig. 5. The QFT-based technique uses fewer circuit samples than the conventional approach, since a comprehensive probability distribution is not reconstructed

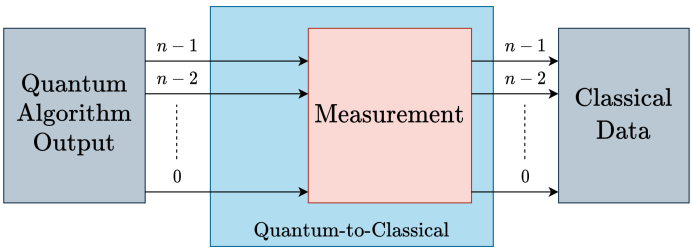

Fig. 4: Procedure for conventional Q2C data decoding

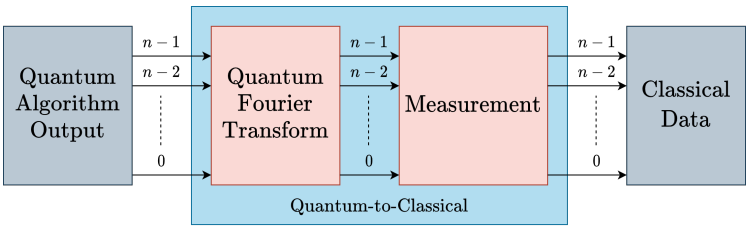

Fig. 5: Procedure for QFT-based Q2C data decoding

but only the Fourier basis states are measured. Data decoding using QFT is particularly relevant for image or audio processing applications, where spectral bandwidth, as an example of a collective property, is useful for analyzing the output data [14]. However, a drawback of the technique is that it does not decode the actual data from its quantum state and only reveals the sought collective property or feature of data. Moreover, the complexity and poor parallelism of the QFT algorithm also results in deep circuits and large overall timing overhead in the circuit.

In our previous work [8], we introduced packet and pyramidal decomposable quantum Haar transform (QHT) circuits for performing quantum-to-classical (Q2C) data decoding. By applying multilevel-decomposable QHT, data represented by n qubits can be transformed to a form represented by a fewer number of qubits $k = n - (\ell \cdot d)$, where $0 \leq k \leq n$, $0 \leq \ell \leq (n/d)$ is the number of decomposition levels, and $d \geq 1$ is the dimensionality of the data. In this work, we extend and optimize the packet and pyramidal circuits and propose a new measurement-based decomposable QHT technique of zero gate depth. We also present comprehensive experimental evaluations of all proposed quantum circuits using real, high-resolution RGB images. In addition, we apply multilevel inverse QHT to reconstruct the decomposed data and evaluate the result fidelity of the Q2C methods in terms of similarity metrics such as data correlation.

3 Proposed Methodology and Circuits

This section outlines our proposed and optimized QHT-based methods and circuits for data decoding in context of the general Q2C approach discussed previously. We first describe the basic QHT circuit for single-level, d-dimensional decomposition. Following

that, we present three methods that extend the single-level operation over multiple decomposition levels and discuss their corresponding quantum circuits.

3.1 Methodology

The quantum Haar transform (QHT) provides a number of benefits for our quantum-to-classical (Q2C) data decoding method. More specifically, QHT preserves the spatial and temporal locality of data such that the decomposed data possesses a spatial and temporal resemblance to the original data [16]. Additionally, QHT is generalizable for multidimensional data, decomposable for multiple levels, and can be implemented with relatively shallow and parallel circuits.

By leveraging multidimensional multilevel-decomposable QHT, we can inherently perform dimension reduction (decompression) of data while preserving its general spatial and temporal characteristics. In other words, QHT allows us to decode data at a decreased qubit cost/count from n qubits to $k = n - (\ell \cdot d)$ qubits, where $0 \leq k \leq n$, $0 \leq \ell \leq (n/d)$ is the number of decomposition levels, and $d \geq 1$ is the dimensionality of the data, e.g., $d = 1$ for 1-D data, $d = 2$ for 2-D data, $d = 3$ for 3-D data, etc. Reducing the number of qubits used in data representation will subsequently reduce the measurement and data decoding time. The proposed methodology for QHT-based Q2C data decoding is shown in Fig. 6.

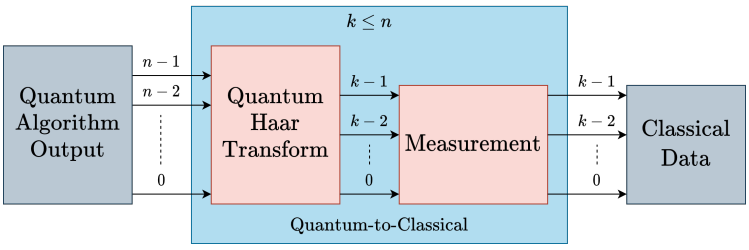

Fig. 6: Procedure for QHT-based Q2C data decoding

3.2 Proposed Quantum Circuits

The QHT algorithm can be represented by a generalized d-dimensional operation denoted as $U^{d-D-QHT}$ henceforth, as depicted in Fig. 7. When encoding multidimensional data as the state amplitudes, a contiguous subset of n_i qubits is used to represent the ith dimension of data, where $0 \leq i < d$. As shown in Fig. 7, $U^{d-D-QHT}$ performs a single level of decomposition over all d dimensions in parallel. It applies a Hadamard (H) gate at the least-significant qubit of every dimension to extract both the low-frequency (slow-changing) and high-frequency (fast-changing) components of the input data followed by a RoR (perfect-shuffle) operation to spatially separate the low-frequency components from the high-frequency components [8]. It is worth mentioning that the low-frequency components constitute a compressed and an approximate version of the original data represented at a lower-resolution, i.e., using less number of

data samples. To decode both the low-frequency and high-frequency components of data, all n qubits must be fully-measured. However, the low-frequency components are usually desired and it is sufficient to partially-measure only the $n_i - 1$ least significant qubits for each dimension, which now contain the low-frequency components after the perfect-shuffle operation, see Fig. 7.

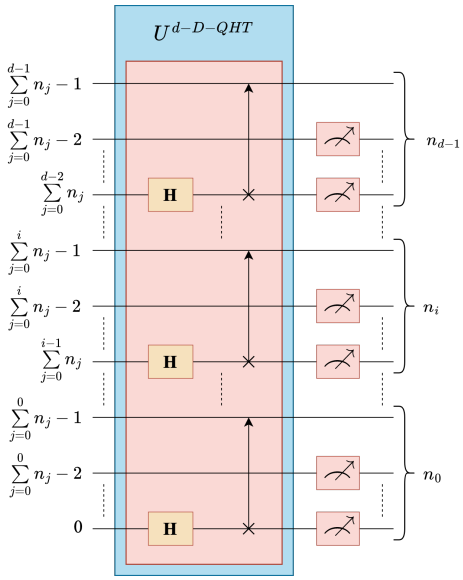

Fig. 7: Single-level decomposition of d-dimensional QHT

As shown in Fig. 7, every contiguous n_i qubits, that are used for encoding the ith data dimension, contain one H gate followed in series by $n_i - 1$ SWAP gates that perform the RoR gate. Therefore, the depth δ of the $U^{d-D-QHT}$ operation can be determined by the depth of the critical path across all dimensions, as shown in (7). The execution time t of the $U^{d-D-QHT}$ operation on a physical quantum hardware can be estimated using the gate delays τ_{H} and τ_{SWAP} of the H and SWAP gates, respectively, as expressed by (8).

$$\delta \equiv \max\{1 + (n_i - 1) : i \in \mathbb{Z}, 0 \leq i < d\} = n_{\max} \tag{7}$$

$$t = \tau_{\mathrm{H}} + (\delta - 1) \cdot \tau_{\mathrm{SWAP}} \tag{8}$$

It is useful to determine the maximum number of levels $\ell_{\max}$ of lossless decomposition. Assuming that decomposition is symmetrically performed on all data dimensions, $\ell_{\max}$ is bound by the number of qubits $n_{\min}$ that are used to encode the data dimension of the least amount of data samples, see (9).

$$\ell_{\max} = n_{\min} \equiv \min\{n_i : i \in \mathbb{Z}, 0 \leq i < d\} \tag{9}$$

3.2.1 Interleaved Packet Decomposition

The multilevel packet decomposition variant of QHT repeatedly applies the $U^{d-D-QHT}$ operation over all qubits for each level of decomposition, as shown in Fig. 8. Here, we leverage and extend our previous work [8, 11] where we presented equations for deriving the circuit depth and the hardware execution time of the packet decomposition circuit when the $U^{d-D-QHT}$ are applied in series. However, the $U^{d-D-QHT}$ operations can be interleaved (overlapped) to further minimize the overall circuit depth. The optimized circuit for packet decomposition incurs only two additional layers of SWAP gates for every additional interleaved level of decomposition, which is reflected in the expressions of (10) and (11) for the circuit depth and execution time, respectively.

$$\delta_{pkt} = n_{\max} + 2(\ell - 1) \tag{10}$$

$$\begin{aligned} t_{pkt} &= \tau_{\mathrm{H}} + (n_{\max} + \ell - 2) \cdot \tau_{\mathrm{SWAP}} + (\ell - 1) \cdot \max(\tau_{\mathrm{H}}, \tau_{\mathrm{SWAP}}) \\ &= \tau_{\mathrm{H}} + (\delta_{pkt} - 1) \cdot \tau_{\mathrm{SWAP}} \end{aligned} \tag{11}$$

$$U_{packet}^{d-D-QHT} = \prod_{k=\ell-1}^{0} U^{d-D-QHT} = (U^{d-D-QHT})^{\ell}$$

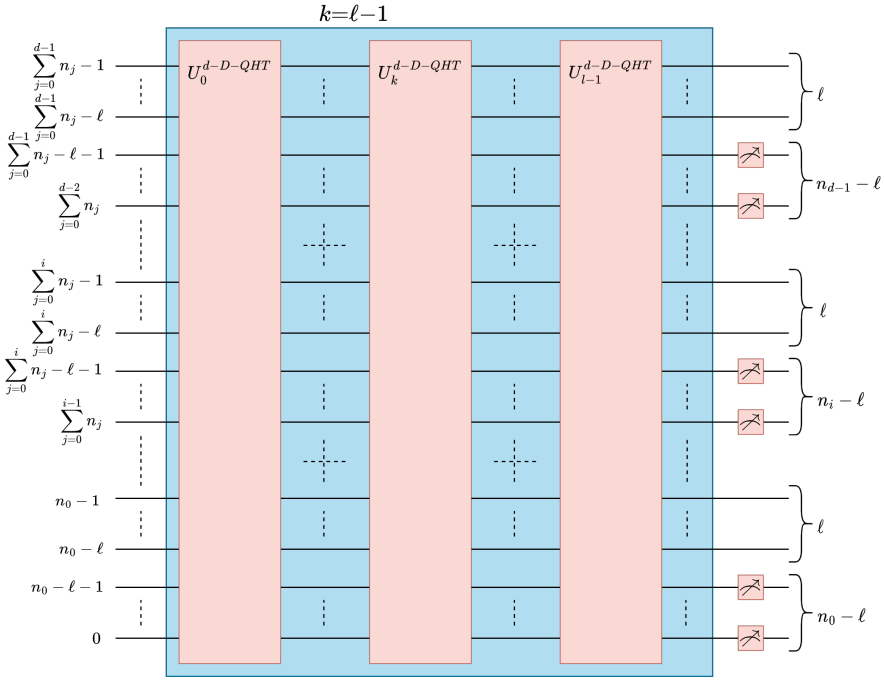

Fig. 8: ℓ-level, d-dimensional packet decomposition

3.2.2 Interleaved Pyramidal Decomposition

In pyramidal decomposition, $U^{d-D-QHT}$ is applied on d fewer data qubits (1 qubit per each dimension) for every level of decomposition, as shown in Fig. 9a. While reducing the size of $U^{d-D-QHT}$ would present tangible benefits to overall circuit size and depth compared to packet decomposition, additional interlevel permutations are required to preserve data locality among the different levels of decomposition, see Fig. 9b.

Similar to packet decomposition as discussed in Section 3.2.1, we could interleave (overlap) the operations of pyramidal decomposition. When interleaved, the second level of decomposition, i.e., $\ell = 2$, adds $n - n_{\max} - d + 2$ additional gate layers to the depth of the first level of decomposition that is comprised of the $U^{d-D-QHT}$ operation and the first set of interlevel permutations. Each following level of decomposition, i.e., $\ell > 2$, adds an additional d gate layers to the overall circuit depth. Accordingly, the total depth of the interleaved pyramidal QHT decomposition, δ_{pyr}, could be expressed by (12), and consequently the execution time is given by (13).

$$\delta_{pyr} = \begin{cases} n_{\max}, & \ell = 1 \\ n + d(\ell - 1) - 2(d - 1), & \ell > 1 \end{cases} \tag{12}$$

$$t_{pyr} = \tau_{\mathrm{H}} + (\delta_{pyr} - 1) \cdot \tau_{\mathrm{SWAP}} \tag{13}$$

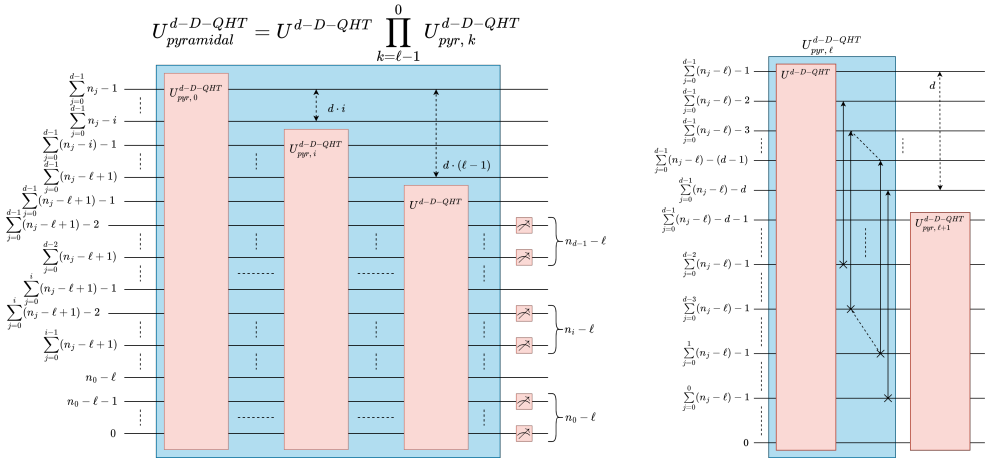

(a) Structure of pyramidal decomposition

(b) Interlevel permutations

Fig. 9: ℓ-level, d-dimensional pyramidal decomposition

3.2.3 Measurement-based Decomposition

The packet and pyramidal circuits are well-optimized for performing a generalized QHT operation: decomposing and spatially separating low-frequency and high-frequency components of multidimensional data as an inherent quantum operation. In the broader context of QHT-based Q2C data decoding, however, additional optimizations are also feasible, and hence we propose our measurement-based decomposition technique.

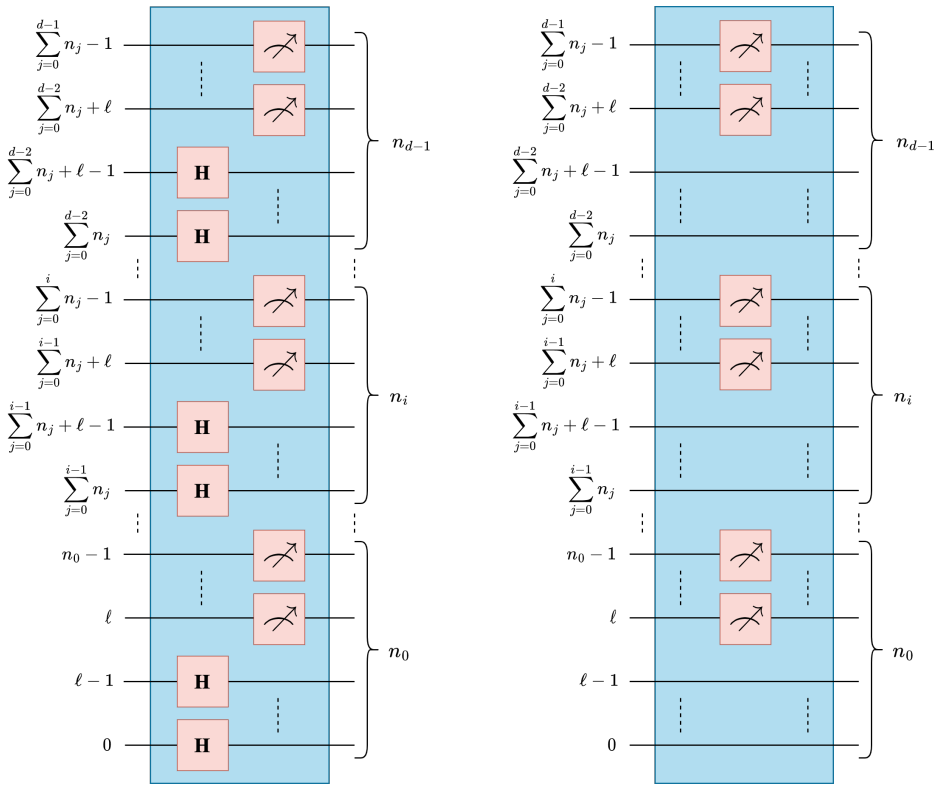

(a) Single-gate depth with H gates (b) Zero-depth circuit

Fig. 10: ℓ-level, d-dimensional measurement-based decomposition

As discussed in Section 3.2, the RoR (perfect-shuffle) operation in $U^{d-D-QHT}$ is useful for spatially separating the low-frequency from high-frequency components in the decomposed quantum state while preserving the data locality. After applying the Hadamard (H) gate in the $U^{d-D-QHT}$ operation, see Fig. 7, the state amplitudes alternate between low-frequency (even indices) and high-frequency (odd indices) terms. Right-rotating (RoR) the qubits for every dimension, i.e., moving the least-significant qubit to the most-significant qubit as shown in Fig. 7, spatially combines/clusters

similar frequency terms together during measurements. Therefore, optimizing out all perfect-shuffle gates would not affect the overall data transformation. However, it reduces the overall depth of the packet and pyramidal QHT circuits resulting in the circuit shown in Fig. 10a. The resulting circuit is composed of $\ell \cdot d$ parallel H gates spanning the ℓ least-significant qubits in each dimension for an ℓ-level, d-dimensional decomposition. The simplified circuit is noteworthy for having a constant circuit depth of 1 H gate independent of the number of decomposition levels.

As shown in Fig. 11a, when an H gate is applied to the least-significant qubit of an n-qubit state $|\psi_n\rangle$ as described by (1), the the resultant state could be represented by $\left|\psi_n^H\right\rangle$ whose full-measurement probability distribution $P(\psi_n^H)$ is given in (14a). Furthermore, (14b) and Fig. 11b display the partial-measurement conditional probability distribution of $\left|\psi_n^H\right\rangle$ when the least-significant qubit q_0 is excluded from measurements after applying the H gate.

$$P\left(\psi_n^H\right) = \begin{bmatrix} p_0 \\ p_1 \\ \vdots \\ p_{2i} \\ p_{2i+1} \\ \vdots \\ p_{N-2} \\ p_{N-1} \end{bmatrix} = \frac{1}{2} \begin{bmatrix} |c_0 + c_1|^2 \\ |c_0 - c_1|^2 \\ \vdots \\ \left|c_{2i} + c_{2i+1}\right|^2 \\ \left|c_{2i} - c_{2i+1}\right|^2 \\ \vdots \\ \left|c_{N-2} + c_{N-1}\right|^2 \\ \left|c_{N-2} - c_{N-1}\right|^2 \end{bmatrix}, \text{ where} \tag{14a}$$

$$P(\psi_n^H = 2i) = p_{2i} = \frac{1}{2}\left|c_{2i} + c_{2i+1}\right|^2,$$

$$P(\psi_n^H = 2i+1) = p_{2i+1} = \frac{1}{2}\left|c_{2i} - c_{2i+1}\right|^2, \text{ and } 0 \leq i < \frac{N}{2}$$

$$\begin{aligned} P\left(\psi_n^H \mid q_0 = \times\right) &= \begin{bmatrix} p_{0|q_0} \\ \vdots \\ p_{i|q_0} \\ \vdots \\ p_{\frac{N}{2}-1|q_0} \end{bmatrix} = \frac{1}{2} \begin{bmatrix} |c_0 + c_1|^2 + |c_0 - c_1|^2 \\ \vdots \\ |c_{2i} + c_{2i+1}|^2 + |c_{2i} - c_{2i+1}|^2 \\ \vdots \\ \left|c_{N-2} + c_{N-1}\right|^2 + \left|c_{N-2} - c_{N-1}\right|^2 \end{bmatrix} \\ &= \begin{bmatrix} |c_0|^2 + |c_1|^2 \\ \vdots \\ |c_{2i}|^2 + |c_{2i+1}|^2 \\ \vdots \\ \left|c_{N-2}\right|^2 + \left|c_{N-1}\right|^2 \end{bmatrix} = P\left(\psi_n \mid q_0 = \times\right), \text{ where} \end{aligned} \tag{14b}$$

$$P(\psi_n^H = i \mid q_0 = \times) = p_{i|q_0} = |c_{2i}|^2 + |c_{2i+1}|^2, \text{ and } 0 \leq i < \frac{N}{2}$$

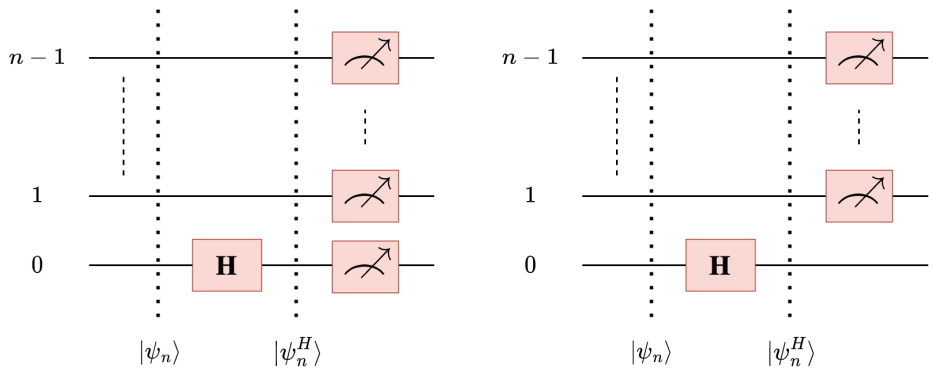

(a) Full-measurement of n qubits

(b) Partial-measurement of $n-1$ qubits

Fig. 11: Measurements of the n-qubit quantum state $\left|\psi_n^H\right\rangle$

It could be concluded based on (14b) and (5b), that the circuits shown in Fig. 11b and Fig. 2b are equivalent where the H gate is effectively non-existent. As such, when performing QHT-based Q2C data decoding and only measuring the low-frequency qubits, it is possible to ignore the H gates and create a circuit that can perform decomposition using only measurement gates as shown in Fig. 10b. Therefore, such a zero-depth circuit allows us to perform dimensionally-reduced Q2C data decoding using ℓ-level, d-dimensional QHT by conducting partial-measurements while excluding the ℓ least-significant qubits per every d dimension of the data, see Fig. 10b.

Note, however, that the zero-depth circuit is restricted only to decomposition, i.e., partially-measuring k qubits from an n-qubit state, where $0 \leq k \leq n$. When performing reconstruction via inverse-QHT, the Hadamard gates will be necessary to restore the high-frequency components in accurate and full data reconstruction/recovery.

4 Experimental Results

The efficacy of our proposed QHT-based Q2C data decoding methods was verified by encoding various sizes of 3D data (RGB images) on both quantum simulators and actual quantum hardware followed by applying QHT for various levels of decomposition. The circuits ranged in size from 8 qubits to 26 qubits to encode multispectral, high-resolution images of $(8 \times 8 \times 3)$ to $(4096 \times 4096 \times 3)$ pixels. The QHT operation was restricted to two dimensions (length and width) to facilitate the maximum possible number of decomposition levels, see (9). In other words, QHT was performed only on the spatial dimensions of the images, not the color bands. Note that with only three color bands (red, green, blue), the statevector was padded with zeroes to comprise a fourth color band, since 2 qubits were required to represent the color dimension, i.e., $n_2 = \lceil \log_2 3 \rceil = 2$. The QHT-based Q2C methods were evaluated for their circuit depth and execution time as reported by the `Qiskit` SDK from IBM Quantum

[13, 19]. Images were also reconstructed from the decomposed images then compared to the original using the Pearson correlation coefficient [20].

In addition, experiments using conventional and QFT-based Q2C data decoding were performed on the same dataset for comparison against the QHT-based techniques. Conventional Q2C data decoding was implemented by measuring all qubits in each circuit and was evaluated in terms of Pearson correlation and hardware execution time, see Figs. 14 to 18. Using the QFT implementation built into `Qiskit` [21], we were able to evaluate QFT-based Q2C in terms of circuit depth and execution time, see Table 1 and Fig. 17, respectively.

All Q2C methods were implemented on `Qiskit` version 0.39.4 [13]. Simulation results were collected using the Aer simulator on a dedicated node of a high-performance computing (HPC) cluster at the University of Kansas (KU). The cluster node used for our experiments is configured with two 12-core Intel Xeon E5-2680 v3 CPUs operating at a base clock of 2.50GHz, PCIe Gen 3.0 connectivity, and 503GB of available memory configured as 8×64GB physical DDR4 DIMMs operating at 2,133MHz. Experiments on actual quantum hardware were performed on *ibmq_toronto*, an IBM Quantum Falcon r4 processor equipped with 27 qubits [22]. The quantum device has a median CNOT error of 1.065×10^{-2}, median readout error of 2.360×10^{-2}, median T1 of 105.97 μs, and median T2 of 101.9 μs [22].

4.1 Accuracy of Quantum Haar Transform

During decomposition, information degradation arises from the loss of high-frequency components after each level of QHT, compounded by additional losses due to typical gate noise and statistical errors of quantum circuits. Experimental correlation results were gathered to quantify information loss for $32,000$ shots (the maximum available on *ibmq_toronto*) and $1,000,000$ shots (the maximum available for simulation), see Figs. 12 and 13, respectively. The decomposed images were reconstructed to calculate their correlation with the original images at the same resolution. Reconstruction was performed classically using a kernel-based method of inverse 2D-QHT to mitigate the introduction of further errors. As such, execution times are not considered for reconstruction.

Differences in correlation among the QHT-based techniques, i.e., packet, pyramidal, and measurement-based, were negligible and therefore they were represented by a single plot named 'QHT-based Q2C' in Figs. 14 and 15. Two additional plots were included as points of comparison. First, we included the correlation from the conventional circuit sampling behavior, see Fig. 4. Next, we repeated these experiments on a classical computer using the classical Haar wavelet transform to isolate the information loss native to the algorithm without the effects of gate errors, decoherence, and sampling errors. Pearson correlation, as a metric for similarity, could not be calculated for QFT-based Q2C data decoding due to the fact that QFT does not preserve the spatial and/or temporal locality of the data.

The quantitative correlation improvement seen from increasing the number of shots between Figs. 14b and 15b can be observed qualitatively from Figs. 12 and 13. When the number of shots is insufficient to sample a quantum state, the measured image appears black, which is seen at $\ell = 3$ for $32,000$ shots but not for $1,000,000$ shots.

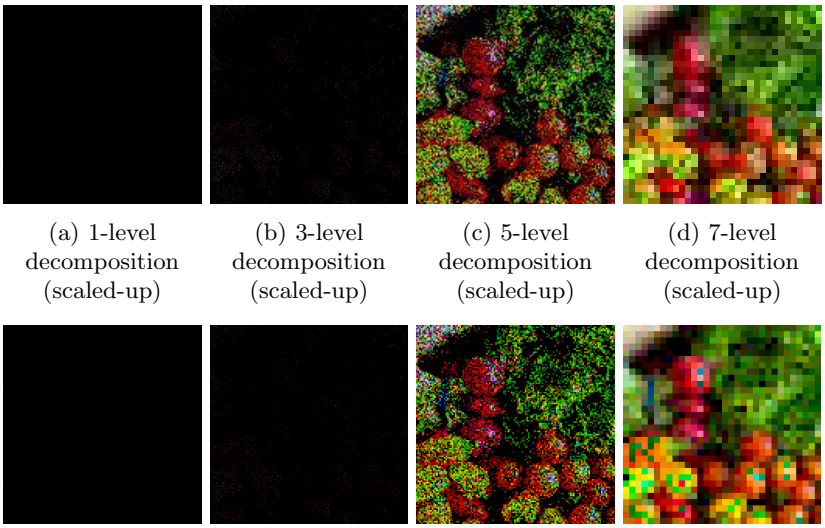

(a) 1-level decomposition (scaled-up) (b) 3-level decomposition (scaled-up) (c) 5-level decomposition (scaled-up) (d) 7-level decomposition (scaled-up)

(e) 1-level reconstruction (f) 3-level reconstruction (g) 5-level reconstruction (h) 7-level reconstruction

Fig. 12: Simulated 2D-QHT decomposition and reconstruction of a $(4096 \times 4096 \times 3)$ image (32,000 shots)

(a) 1-level decomposition (scaled-up) (b) 3-level decomposition (scaled-up) (c) 5-level decomposition (scaled-up) (d) 7-level decomposition (scaled-up)

(e) 1-level reconstruction (f) 3-level reconstruction (g) 5-level reconstruction (h) 7-level reconstruction

Fig. 13: Simulated 2D-QHT decomposition and reconstruction of a $(4096 \times 4096 \times 3)$ image (1,000,000 shots)

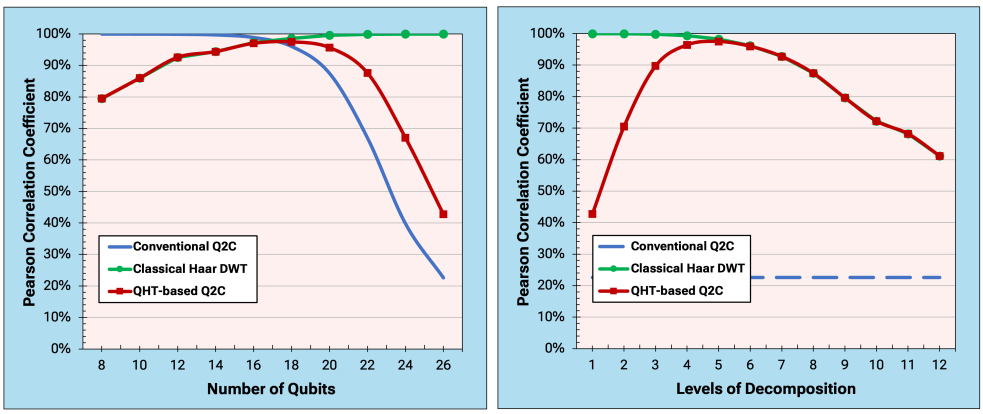

(a) 1-level decomposition (b) 26-qubit state

Fig. 14: Correlation of reconstructed 2D-QHT images on Aer simulator with 32,000 shots

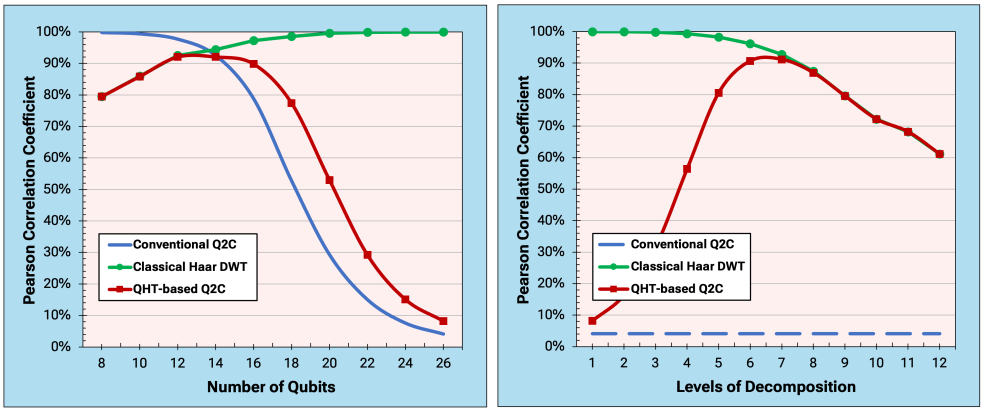

(a) 1-level decomposition (b) 26-qubit state

Fig. 15: Correlation of reconstructed 2D-QHT images on Aer simulator with 1,000,000 shots

Taken together, Figs. 14 and 15 illustrate the interaction between information loss from the QHT algorithm and information loss from sampling errors. The results for conventional Q2C data decoding in Figs. 14a and 15a highlight a distinct logistic relationship between the number of qubits and/or shots with the correlation of the measured quantum state. Below a certain proportion of shots to image size, the correlation displays a 'saturation' behavior, where increasing the number shots or decreasing the image size has a negligible impact on the correlation. This is indicative that the number of shots is already sufficient to characterize the expected quantum state. The classical

Haar wavelet transform shows similar logistic behavior, although higher correlation is observed for larger image sizes, where removing high-frequency terms presents a smaller impact.

From Figs. 14a and 15a, as the image size increases for a fixed number of decompositions, we observe that the QHT correlation aligns strongly with the classical wavelet plot, demonstrating how the algorithmic component of information loss dominates within the saturation region. Outside of that region, the information loss from sampling a larger image dramatically outweighs the relative gain in correlation from performing the Haar transform on a larger image. Similar behavior extends to applying different levels of decomposition to fixed-size images as shown in Figs. 14b and 15b. Beyond a certain number of decomposition levels, only few qubits are being measured such that we enter the saturation region for a given number of shots. Thus, the correlation aligns with the expected behavior from the classical Haar transform. However, before that point, the comparatively small information loss from the Haar transform helps ameliorate the dramatic information loss from measuring such a large image.

Given a large enough image for a certain number of shots, the QHT-based Q2C method can outperform conventional Q2C data decoding in terms of the quality of results (fidelity) with the improvement increasing as fewer shots are performed, as shown in Fig. 16. As the image sizes increase, the rate of correlation improvement increases until all levels of decomposition outperform the conventional decoding technique once $n \geq 18$ for $32,000$ shots and $n \geq 22$ for $1,000,000$ shots. The largest improvement is seen when $n = 26$, $\ell = 7$ for $32,000$ shots, where the 2D-QHT circuit returned a 91.18% correlation coefficient compared to a 4.12% correlation coefficient for conventional Q2C, see Figs. 15b and 16a.

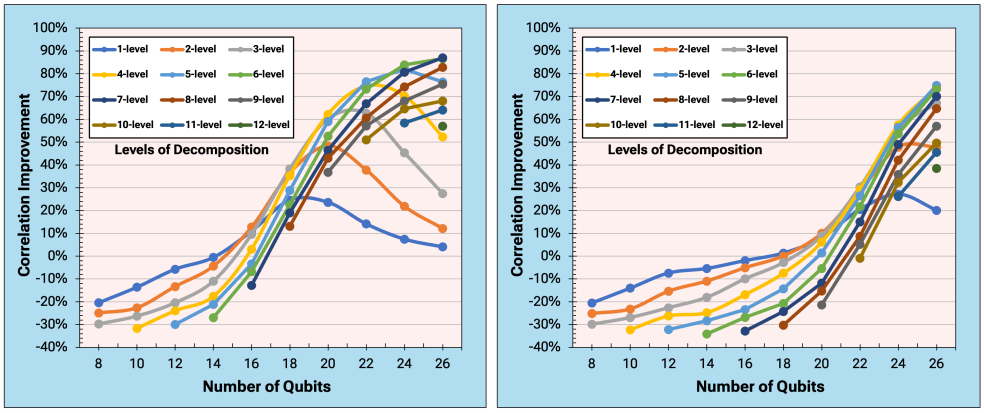

(a) 32,000 shots (b) 1,000,000 shots

Fig. 16: Correlation improvement of 2D-QHT over conventional Q2C on Aer simulator

4.2 Performance of Quantum Haar Transform on Hardware

On quantum simulators, quantum circuits are often preset to their initial state, and accordingly the overhead associated with state synthesis (preparation) is usually ignored. However, on actual quantum hardware, state synthesis requires a deep quantum operation to be applied to the ground $|0\rangle^{\otimes n}$ state. IBM `Qiskit` uses the `Initialize` API [23] to implement state synthesis leveraging a method of depth $\mathcal{O}(2^n)$ [24, 25]. Including state preparation in hardware execution would introduce significant overhead to execution time, obfuscate performance differences between Q2C methods, and restrict experiments to at most 14-qubit states, i.e., images of size $(64 \times 64 \times 3)$ pixels, due to constraints of the IBM Quantum platform. Therefore, Fig. 17 compares the execution times for conventional Q2C, QFT-based Q2C, and QHT-based Q2C methods, excluding state preparation overhead, on the 27-qubit *ibmq_toronto* processor from IBM Quantum [22].

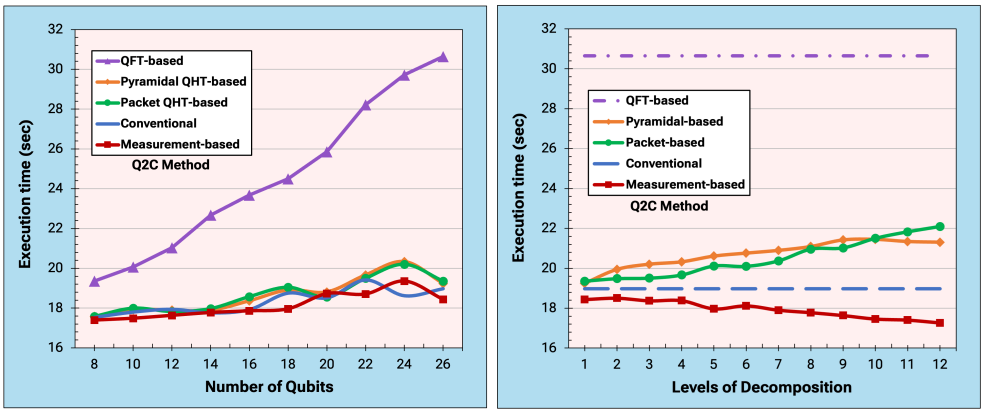

(a) 1-level decomposition (b) 26-qubit state

Fig. 17: Execution times for 2D-QHT decomposition on the 27-qubit *ibmq_toronto* device

Taken together, our results demonstrate QHT-based Q2C data decoding, particularly the measurement-based technique, exhibits significant speedup compared to contemporary Q2C techniques on hardware. Speedup is shown in Fig. 18, where it is calculated as the ratio between the execution time of a contemporary Q2C technique for a given image size and the execution time of the corresponding ℓ-level measurement-based decomposition.

Fig. 18 shows near-universal speedup of the measurement-based QHT technique compared to conventional and QFT-based Q2C data decoding on hardware. In general, we observe higher speedup for larger circuits and more decomposition levels as expected, since the measurement-based QHT technique measures $\ell \cdot d$ fewer qubits than either the conventional or QFT-based Q2C techniques, without using any additional quantum gates. Moreover, these results include circuit-independent overhead

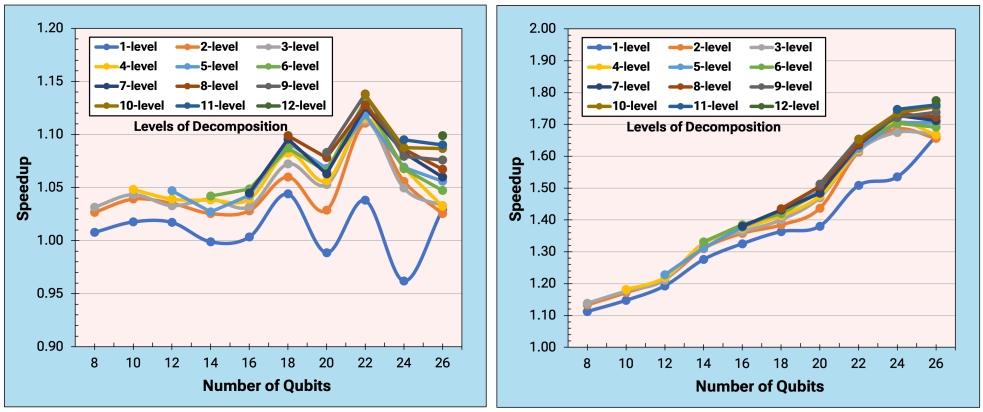

(a) Speedup over conventional Q2C (b) Speedup over QFT-based Q2C

Fig. 18: Speedup of measurement-based 2D-QHT over contemporary Q2C methods on the 27-qubit *ibmq_toronto* device

from resetting qubits to the ground state between shots. If executions were performed restlessly, we should expect to see even greater speedup from the proposed measurement-based Q2C technique over QFT-based Q2C.

4.3 Comparison of Packet and Pyramidal Circuits

The depth analysis provided in [8, 11] for the packet and pyramidal circuits assumes serial execution of each level of decomposition to provide a pessimistic prediction of execution time. While the new analysis in (10) to (13) is more physically accurate, quantum devices also possess unique qubit coupling restrictions requiring additional SWAP operations which are not considered in our analysis. Table 1 presents the circuit depths of the packet and pyramidal decomposition techniques before and after optimization in terms of H and SWAP gates. These values were collected from the `QuantumCircuit.depth()` [19] API in `Qiskit` and align with theoretical expectations from (10) and (12).

Both the packet and pyramidal variants of our proposed QHT-based Q2C techniques have identical circuits at $\ell = 1$ and only become distinct for higher levels of decomposition, i.e., when $\ell > 1$. For the circuits from [8, 11], the pyramidal circuit depth increases quadratically with increasing levels of decomposition, while the packet circuit depth increases linearly. As a result, the pyramidal circuit depth intersects with the packet circuit depth at $\ell_{\max}$, see (9), and would be expected to become shallower if further decomposition levels were possible. By contrast, the proposed packet circuits for multilevel decomposition are strictly shallower than the proposed pyramidal circuits. Overall, the overlapping optimization to the QHT circuits were critical to achieve shallower circuits than QFT for any image size and level of decomposition.

The circuit execution times as modelled by (11) and (13) do not include the overhead associated with the measurement operations (gates), resulting from repeated

Table 1: Depth optimizations for packet and pyramidal 2D-QHT circuits

(a) Packet theoretical circuit depth in terms of H, SWAP, and Controlled-Phase gates

# of Qubits	Reported [8, 11]												Proposed (Interleaved / Overlapped)												QFT
	1-level	2-level	3-level	4-level	5-level	6-level	7-level	8-level	9-level	10-level	11-level	12-level	1-level	2-level	3-level	4-level	5-level	6-level	7-level	8-level	9-level	10-level	11-level	12-level	
8	3	6	9										3	5	7										16
10	4	8	12	16									4	6	8	10									20
12	5	10	15	20	25								5	7	9	11	13								24
14	6	12	18	24	30	36							6	8	10	12	14	16							28
16	7	14	21	28	35	42	49						7	9	11	13	15	17	19						32
18	8	16	24	32	40	48	56	64					8	10	12	14	16	18	20	22					36
20	9	18	27	36	45	54	63	72	81				9	11	13	15	17	19	21	23	25				40
22	10	20	30	40	50	60	70	80	90	100			10	12	14	16	18	20	22	24	26	28			44
24	11	22	33	44	55	66	77	88	99	110	121		11	13	15	17	19	21	23	25	27	29	31		48
26	12	24	36	48	60	72	84	96	108	120	132	144	12	14	16	18	20	22	24	26	28	30	32	34	52

(b) Pyramidal theoretical circuit depth in terms of H, SWAP, and Controlled-Phase gates

# of Qubits	Reported [8, 11]												Proposed (Interleaved / Overlapped)												QFT
	1-level	2-level	3-level	4-level	5-level	6-level	7-level	8-level	9-level	10-level	11-level	12-level	1-level	2-level	3-level	4-level	5-level	6-level	7-level	8-level	9-level	10-level	11-level	12-level	
8	3	7	9										3	6	8										16
10	4	10	14	16									4	8	10	12									20
12	5	13	19	23	25								5	10	12	14	16								24
14	6	16	24	30	34	36							6	12	14	16	18	20							28
16	7	19	29	37	43	47	49						7	14	16	18	20	22	24						32
18	8	22	34	44	52	58	62	64					8	16	18	20	22	24	26	28					36
20	9	25	39	51	61	69	75	79	81				9	18	20	22	24	26	28	30	32				40
22	10	28	44	58	70	80	88	94	98	100			10	20	22	24	26	28	30	32	34	36			44
24	11	31	49	65	79	91	101	109	115	119	121		11	22	24	26	28	30	32	34	36	38	40		48
26	12	34	54	72	88	102	114	124	132	138	142	144	12	24	26	28	30	32	34	36	38	40	42	44	52

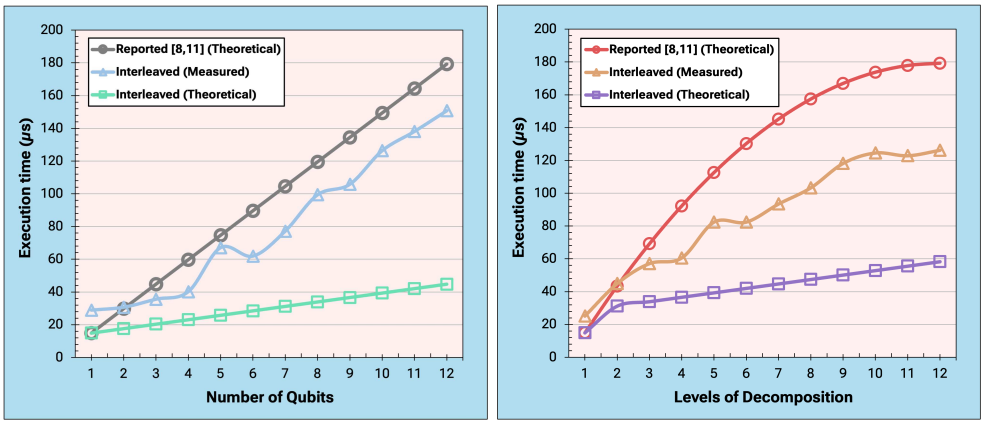

(a) Packet decomposition (b) Pyramidal decomposition

Fig. 19: Expected (theoretical) and measured per-shot execution times of 2D-QHT for 26-qubit circuits

qubit resets among circuit samples (shots). Accordingly, we conducted experiments to determine that overhead and accounted for it in our results by reporting the per-shot execution times, as shown in Fig. 19. After accounting for measurement-gate overhead, the per-shot execution time on hardware for both packet and pyramidal decomposition was upper-bounded by the execution time predictions of the pessimistic sequential model from [8, 12] and lower-bounded by the interleaved/overlapped model presented

in this work, see Fig. 19. Such behavior should be expected, since additional SWAP gates from hardware transpilation were not considered.

The performance of the packet and pyramidal circuits in Figs. 17b and 19 reflect expected behavior for $\ell < 10$ from (11) and (13), due to how the interlevel permutations in pyramidal decomposition undermine the parallelism seen from overlapping levels of packet decomposition, in spite of reducing the size of the $U^{d-D-QHT}$ operator every level of decomposition. However, quantum devices have varying topologies and usually are not fully connected, therefore additional SWAP gates are included during hardware transpilation to compensate for the mismatch between the algorithmic requirements and the target topology of the quantum device. As a result, at higher levels of decomposition, the packet and pyramidal circuits on actual hardware were close to following the reported model in [8, 11], as shown in Figs. 17b and 19.

5 Conclusions and Future Work

Contemporary methods of quantum-to-classical (Q2C) data decoding incur significant time overhead from repeated sampling of the quantum state, making it difficult to practically implement time-efficient quantum algorithms. This work proposed Q2C data decoding methods based on the multidimensional, multilevel-decomposable quantum Haar transform (QHT), including a 'measurement-based' method that requires no additional quantum gates. All methods were implemented on IBM Quantum's `Qiskit` SDK, executed both on a simulator and actual quantum hardware. The experimental results reveal the efficacy of the proposed techniques to improve time efficiency while simultaneously improving measurement accuracy. In our future work, we will leverage our proposed QHT-based Q2C techniques for data-intensive applications such as quantum machine learning (QML). We will also investigate the effect of different topologies of quantum devices on the performance of quantum algorithms.

Acknowledgements

This research used resources of the Oak Ridge Leadership Computing Facility, which is a DOE Office of Science User Facility supported under Contract DE-AC05-00OR22725.

Declarations

Ethical Approval

Not applicable.

Competing interests

No competing interests.

Authors' contributions

- All authors reviewed the manuscript.

- All authors, particularly David Levy, Vinayak Jha, Jack Bauer, and Anshul Maurya, participated in preparing the figures and Tables.
- The lead author, Mingyoung Jeng lead the effort of conducting the experimental work with SM Ishraq Ul Islam, Manu Chaudhary, Md. Alvir Islam Nobel, and Dylan Kneidel.
- The lead author, Mingyoung Jeng, and Andrew Riachi, participated in developing the analytical models, writing the coding scripts, and analyzing and discussing the experimental data.
- Esam El-Araby and Naveed Mahmud generated the idea for this work, and developed the initial system design and code.
- Esam El-Araby guided the direction of the paper, and ensured that the quality of its contribution was sufficient for publication.

Funding

Not applicable.

Availability of data and materials

Not applicable.

References

[1] Troels F Rønnow, Zhihui Wang, Joshua Job, Sergio Boixo, Sergei V Isakov, David Wecker, John M Martinis, Daniel A Lidar, and Matthias Troyer. Defining and detecting quantum speedup. *science*, 345(6195):420–424, 2014.

[2] Peter W Shor. Polynomial-time algorithms for prime factorization and discrete logarithms on a quantum computer. *SIAM review*, 41(2):303–332, 1999.

[3] Lov K Grover. Quantum mechanics helps in searching for a needle in a haystack. *Physical review letters*, 79(2):325, 1997.

[4] Wen Guan, Gabriel Perdue, Arthur Pesah, Maria Schuld, Koji Terashi, Sofia Vallecorsa, and Jean-Roch Vlimant. Quantum machine learning in high energy physics. *Machine Learning: Science and Technology*, 2(1):011003, 2021.

[5] John Preskill. Quantum computing in the nisq era and beyond. *Quantum*, 2:79, 2018.

[6] Manuela Weigold, Johanna Barzen, Frank Leymann, and Marie Salm. Data encoding patterns for quantum computing. In *HILLSIDE Proc. of Conf. on Pattern Lang. of Prog. 22*, 2020.

[7] Marco Lanzagorta and Jeffrey Uhlmann. Is quantum parallelism real? In *Quantum Information and Computation VI*, volume 6976, page 69760W. International Society for Optics and Photonics, 2008.

[8] Naveed Mahmud, Mingyoung Joshua Jeng, Md. Alvir Islam Nobel, Manu Chaudhary, SM Ishraq Ul Islam, David Levy, and Esam El-Araby. Time-efficient quantum-to-classical data decoding. In *The International Conference on Emergent Quantum Technologies (ICEQT 2022), Las Vegas, Nevada, USA, July*

2022. To appear in Transactions on Computational Science & Computational Intelligence, Springer Nature - Research Book Series, 2022.

[9] Amir Fijany and Colin P Williams. Quantum wavelet transforms: Fast algorithms and complete circuits. In *NASA international conference on quantum computing and quantum communications*, pages 10–33. Springer, 1998.

[10] Hai-Sheng Li, Ping Fan, Huiling Peng, Shuxiang Song, and Gui-Lu Long. Multilevel 2-D Quantum Wavelet Transforms. *IEEE Transactions on Cybernetics*, 2021.

[11] Naveed Mahmud, Andrew Macgillivray, Manu Chaudhary, and Esam El-Araby. Decoherence-optimized circuits for multi-dimensional and multi-level decomposable quantum wavelet transform. *IEEE Internet Computing (IEEE IC) Special Issue on Quantum and Post-Moore's Law Computing*, 26(01):15–25, 2022.

[12] Naveed Mahmud, Bennett Haase-Divine, Andrew MacGillivray, and Esam El-Araby. Quantum dimension reduction for pattern recognition in high-resolution spatio-spectral data. *IEEE Transactions on Computers*, 71(1):1–12, 2020.

[13] IBM Quantum. Qiskit: An open-source framework for quantum computing, 2021.

[14] Colin P. Williams and Scott H. Clearwater. *Explorations in quantum computing*. Springer, 1998.

[15] Chi Zhang, Yanhao Chen, Yuwei Jin, Wonsun Ahn, Youtao Zhang, and Eddy Z Zhang. A depth-aware swap insertion scheme for the qubit mapping problem. *arXiv preprint arXiv:2002.07289*, 2020.

[16] Esam El-Araby, Tarek El-Ghazawi, Jacqueline Le Moigne, and Kris Gaj. Wavelet spectral dimension reduction of hyperspectral imagery on a reconfigurable computer. In *Proceedings. 2004 IEEE International Conference on Field-Programmable Technology (IEEE Cat. No. 04EX921)*, pages 399–402. IEEE, 2004.

[17] S. Kaewpijit, J. Le Moigne, and T. El-Ghazawi. Automatic reduction of hyperspectral imagery using wavelet spectral analysis. *IEEE Transactions on Geoscience and Remote Sensing*, 41(4):863–871, 2003.

[18] Mladen Victor Wickerhauser. *Adapted Wavelet Analysis: From Theory to Software*. Routledge, 1994.

[19] IBM Quantum. QuantumCircuit.depth() [computer software]. https://qiskit.org/documentation/stubs/qiskit.circuit.QuantumCircuit.depth.html, 2023. [Online] Accessed: 2023-03-31.

[20] Karl Pearson. Note on regression and inheritance in the case of two parents. *Proceedings of the Royal Society of London*, 58:240–242, 1895.

[21] IBM Quantum. QFT [computer software]. https://qiskit.org/documentation/stubs/qiskit.circuit.library.QFT.html, 2023. [Online] Accessed: 2023-03-31.

[22] IBM Quantum. https://quantum-computing.ibm.com/, 2023. [Online] Accessed: 2023-03-31.

[23] IBM Quantum. Initialize [computer software]. https://qiskit.org/documentation/stubs/qiskit.extensions.Initialize.html, 2023. [Online] Accessed: 2023-03-31.

[24] IBM Quantum. StatePreparation [computer software]. https://qiskit.org/documentation/stubs/qiskit.circuit.library.StatePreparation.html, 2023. [Online] Accessed: 2023-03-31.

[25] V.V. Shende, S.S. Bullock, and I.L. Markov. Synthesis of quantum-logic circuits. *IEEE Transactions on Computer-Aided Design of Integrated Circuits and Systems*, 25(6):1000–1010, 2006.